Umar Faroog Ghumman¹

Mechanical Engineering, Northwestern University, 2145 Sheridan Road, Evanston, IL 60208 e-mail: umarghumman2018@u.northwestern.edu

Akshay Iyer¹

Mechanical Engineering, Northwestern University, 2145 Sheridan Road, Evanston, IL 60208 e-mail: akshayiyer2021@u.northwestern.edu

Rabindra Dulal

Physics and Astronomy, University of Wyoming, 1000 E. University, Dept 3905, Laramie, WY 82071 e-mail: rdulal@uwyo.edu

Joydeep Munshi

Mechanical Engineering and Mechanics, Lehigh University, Packard Lab 367, 19 Memorial Drive West, Bethlehem, PA 18015 e-mail: jom317@lehigh.edu

Aaron Wang

Physics and Astronomy, University of Wyoming, 1000 E. University, Dept 3905, Laramie, WY 82071 e-mail: swang9@uwyo.edu

TeYu Chien

Physics and Astronomy, University of Wyoming, 1000 E. University, Dept 3905, Laramie, WY 82071 e-mail: tchien@uwyo.edu

Ganesh Balasubramanian

Mechanical Engineering and Mechanics, Lehigh University, Packard Lab 561, 19 Memorial Drive West, Bethlehem, PA 18015 e-mail: bganesh@lehigh.edu

Wei Chen²

Mechanical Engineering, Northwestern University, 2145 Sheridan Road, Evanston, IL 60208 e-mail: weichen@northwestern.edu

A Spectral Density Function Approach for Active Layer Design of Organic Photovoltaic Cells

Organic photovoltaic cells (OPVCs), having received significant attention over the last decade, are yet to be established as viable alternatives to conventional solar cells due to their low power conversion efficiency (PCE). Complex interactions of several phenomena coupled with the lack of understanding regarding the influence of fabrication conditions and nanostructure morphology have been major barriers to realizing higher PCE. To this end, we propose a computational microstructure design framework for designing the active layer of P3HT:PCBM based OPVCs conforming to the bulk heterojunction (BHJ) architecture. The framework pivots around the spectral density function (SDF), a frequency space microstructure characterization, and reconstruction methodology, for microstructure design representation. We validate the applicability of SDF for representing the active layer morphology in OPVCs using images of the nanostructure obtained by cross-sectional scanning tunneling microscopy and spectroscopy (XSTM/S). SDF enables a low-dimensional microstructural representation that is crucial in formulating a parametric-based microstructure optimization scheme. A level-cut Gaussian random field (GRF, governed by SDF) technique is used to generate reconstructions that serve as representative volume elements (RVEs) for structure-performance simulations. A novel structure-performance (SP) simulation approach is developed using a physics-based performance metric, incident photon to converted electron (IPCE) ratio, to account for the impact of microstructural features on OPVC performance. Finally, a SDF-based computational IPCE optimization study incorporating only three design variables results in 36.75% increase in IPCE, underlining the efficacy of the proposed design framework. [DOI: 10.1115/1.4040912]

1 Introduction

Design of nanostructured material systems (NMSs) [1] has recently gained impetus due to its potential for developing high performance metamaterials by cost-effective nanofabrication techniques [2–6]. A convenient way of categorizing NMSs is based on the presence of periodicity in the morphology. Periodic

Journal of Mechanical Design

Copyright © 2018 by ASME

¹U. F. Ghumman and A. Iyer contributed equally to this work.

²Corresponding author.

Contributed by the Design Automation Committee of ASME for publication in the JOURNAL OF MECHANICAL DESIGN. Manuscript received March 30, 2018; final manuscript received July 11, 2018; published online September 7, 2018. Assoc. Editor: Carolyn Seepersad.

designs involve deterministic arrangement of identical building blocks (also known as unit cells), with optimal performance realized through evolutionary algorithms [3,7,8] and topology optimization [4,9]. However, fabrication of periodic NMSs requires top-down nanomanufacturing techniques which are often expensive and time consuming to ensure precise material deposition at nano- and microscales [10]. In contrast to periodic NMSs, a quasirandom nanostructure contains no periodic arrangement of unit cells, but a seemingly random material distribution governed by an underlying spatial correlation. Such structures have been observed in nature [11–14] as well as artificially synthesized materials [15–18] using low cost and bottom—up manufacturing processes [19] (which uses atoms/molecules as the building blocks, self-assembled to create complex nanostructures) such as nanowrinkling [2,17].

Organic photovoltaic cells (OPVCs) [20-23] are one such example of man-made quasi-random nanostructures. Owing to a series of advantages such as flexibility, light weight, low production cost, and lack of heavy metals (environmental friendly), OPVCs have received significant attention as one of the promising materials for next generation solar cells [24,25]. The short mean free path (2–10 nm) of the excitons [26] in organic molecules requires that the locations of exciton creation should be in the vicinity of the electron donor-acceptor interface for efficient charge separation. It has been shown that the bulk heterojunction (BHJ) architecture of the active layer is key to ensure high efficiency due to its quasirandom nanostructures satisfying the aforementioned short exciton mean free path limitation [26]. As illustrated in Fig. 1(a), charge separation at the donor-acceptor interfaces and transport to the electrodes are critical to high performance of the device. Among the various electron donor/acceptor combinations investigated previously, phenyl-C61-butyric-acid-methyl ester (PCBM) interspersed with poly(3-hexylthiophene-2,5-diyl) (P3HT) has been the 'best seller" [27]. To achieve optimal power conversion efficiencies (PCEs), several structure and process synthesis parameters, such as electron donor-acceptor composition, thickness of the active layer, annealing temperature, and annealing duration, etc., need to be optimized simultaneously. Previous efforts only focus on one or two structure and processing parameters at a time to search for optimal devices. However, the optimal parameters are not independent from each other, indicating that better strategies

are needed. Currently, there is no reported methodology to consider the influences of all fabrication conditions simultaneously on the microstructures or the influences of the microstructures on the device performance.

To produce cost-effective devices with targeted properties, formulating a holistic material design strategy [28-33] is essential. Since the device's microstructure influences its behavior at different length scales, microstructure mediated design [30,34] or microstructure sensitive design [35] has assumed prime importance. Deconvolving the structure-performance (S-P) relationship has been the focus of many articles, covering a wide range of material systems [36–41]. Due to its high dimensionality, one needs to extract the salient features from a microstructure image before its influences on material behavior can be studied. Microstructure characterization and reconstruction (MCR) [42,43] has enabled a quantitative approach to analyze microstructural images and subsequently construct models for investigating S-P relationship. The essence of MCR is its ability to capture significant microstructural details and subsequently generate statistically equivalent reconstructions. The widely used MCR approaches [42] for nondeterministic systems are based on spatial correlation functions (CRFs) [43-45], descriptor-based methods [40,46], and machine learning techniques [47-49]. The correlation function approach captures the microstructure from a probabilistic perspective but relies on a pixel (voxel in three-dimensional (3D)) swapping strategy for reconstructions and is therefore computationally prohibitive for microstructural design. Descriptor-based approach uses a small set of uncorrelated features which embody significant microstructural detail and has been successfully used for design of nanocomposite polymers [40,46,50-52], that contain clusters of filler material dispersed in the polymer matrix. However, this approach assumes filler aggregates to be ellipsoidal and descriptors are regular geometrical features (aspect ratio, equivalent radius, etc.), thus, falling short in representing arbitrary geometries encountered in quasi-random NMSs. While machine learning methods, which are capable of modeling highly nonlinear systems, have been implemented as MCR tools, the lack of physical interpretation of parameters learned from these methods has limited their use in material design.

Spectral density function (SDF) [2,5,6,53] has emerged as a new method for low-dimensional, physics aware representation of

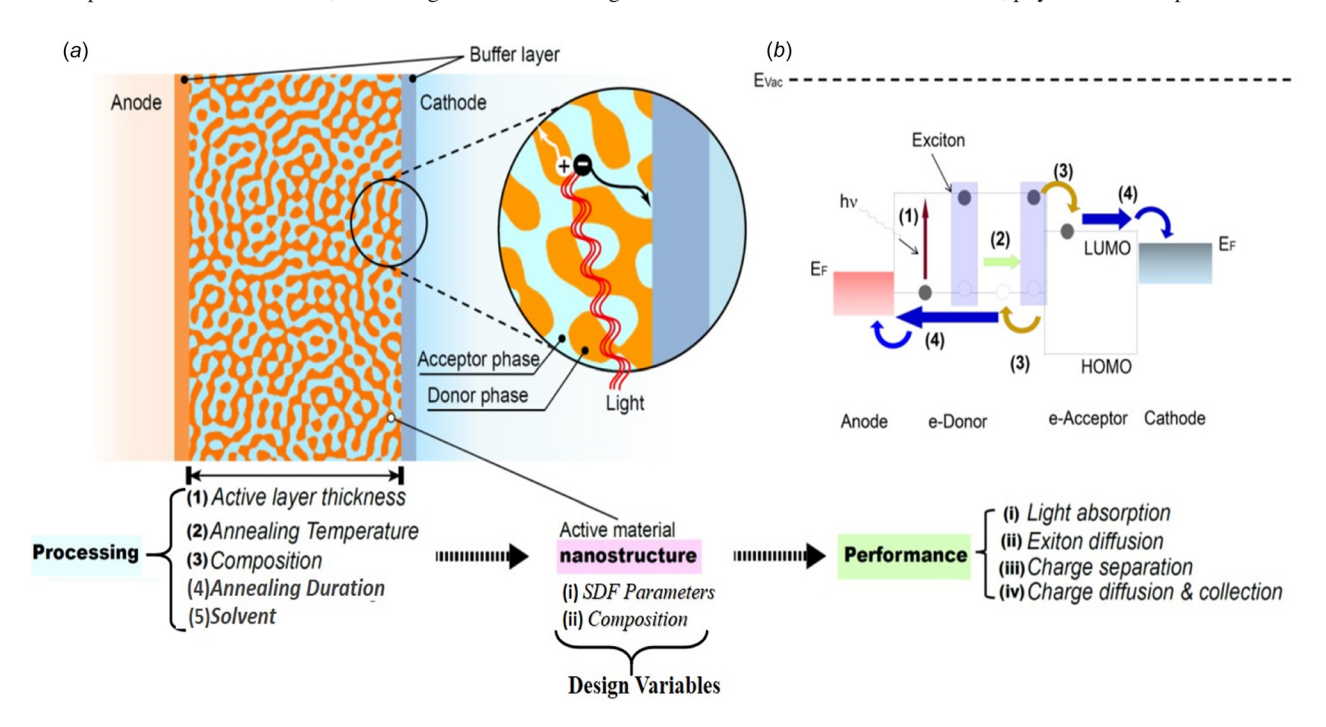


Fig. 1 Variables of interest in processing–structure–performance framework and design scope: (a) A schematic representation of OPVC with BHJ architecture; (b) a four-step energy conversion mechanism

111408-2 / Vol. 140, NOVEMBER 2018

quasi-random NMSs. For isotropic materials, SDF is a onedimensional (1D) function of spatial frequency, calculated as the radial average of the squared magnitude of Fourier spectrum of a quasi-random structure [53] and represents the structural correlation in Fourier space. Analogous to the way correlation functions describe structural correlations in real space, SDF provides this description in reciprocal space. Our previous efforts in design of photonic NMSs with SDF [2,5,6] have highlighted its advantages in representing quasi-random microstructures with a small number of required design variables. Yu et al. [6] presented the first comprehensive MCR study on application of SDF for quasi-random NMSs used as light trapping structure in thin-film solar cells. They showed that low-dimensional microstructure representation enabled by SDF, its direct association with material functionalities and relationship with processing conditions, was instrumental in design optimization and led to a 4.7-fold enhancement of single wavelength light absorption. In another recent article, Lee et al. [2] integrated a novel wafer scale nanofabrication procedure, wrinkle lithography, with SDF-based microstructure representation to bridge the processing–structure and structure–performance relationship for concurrent design of photonic nanostructures. The study showed that parameters in SDFs have physical implications closely associated with the material processing conditions, improving the feasibility of fabricating the optimal nanostructures obtained from computational design methods.

In this paper, we investigate the applicability of SDF for design of the active layer in OPVCs and propose a design framework built on SDF-based S-P evaluations (Sec. 2). Active layer samples comprising P3HT:PCBM and conforming to BHJ architecture are fabricated and imaged using novel cross-sectional scanning tunneling microscopy and spectroscopy (XSTM/S) (Sec. 3). Further, this article focuses on establishing S-P relationship by creating protocols for SDF-based microstructure representation (Sec. 4) and developing a novel, physics-based performance evaluation strategy (Sec. 5). To demonstrate the usefulness of microstructure representation using SDF and the S-P relationship investigated here, we formulate a performance optimization problem to determine the optimal microstructure (Sec. 6). State-of-the-art computational design methods are employed to improve the efficiency of simulation-based design optimization. Specifically, optimal Latin hypercube sampling (OLHS) [54] is used to create a metamodel based on Kriging metamodeling [55], overcoming the challenges of computational cost and time. Finally, Sobol sensitivity analysis [56] is used to elucidate the effect of each design variable (Sec. 7).

2 Spectral Density Function-Based Microstructure Design Framework

Low-dimensional, physics-aware nanostructure representation is critical for computational design of quasi-random NMSs. In this section, we first demonstrate SDF to be a convenient frequency space representation which embodies significant real space features and assumes simple parametric form for isotropic materials. Then, an SDF-based microstructure design framework is presented in the context of active layer design for OPVCs.

2.1 Introduction to Spectral Density Function. The SDF is an analytical tool developed to characterize the structural information of a given material. The backbone of SDF is the Fourier transform (FT) which decomposes a waveform (e.g., 1D signal or a 3D image) into a sum of sinusoidal waves of different frequencies [57]. When the FT operator is applied to a microstructure image, real space structural features are represented in the spatial frequency space and enable identification of spatial correlations. SDF has demonstrated its ability to characterize intricate heterogeneous microstructures as well as generate statistically equivalent reconstructions [42]. For isotropic materials, the shape of radially averaged SDF curve generally takes a simple parametric

form which significantly reduces the design complexity of an otherwise high dimensional material structure.

To characterize a microstructure using SDF, a two-phase image, X, is required. The image must contain high resolution details at the microstructural level. The Fourier transform $F(\mathbf{k})$ of the image is calculated as

$$F(\mathbf{k}) = F[X] = A_{\mathbf{k}} e^{i\phi_{\mathbf{k}}} \tag{1}$$

Here, F[.] represents the FT operator, k is a vector which represents frequency, $i=\sqrt{(-1)}$, and A_k and \emptyset_k represent the magnitude and phase angle of the FT, respectively. For isotropic materials, the vector k can be reduced to a scalar by radially averaging in the spatial frequency domain. Thus, the SDF of the microstructure, $\rho(k)$, is then calculated by radial averaging of the squared magnitude of FT

$$\rho(k) = \frac{\int_0^{2\pi} |F(\mathbf{k})|^2 d\theta}{2\pi} = \frac{\int_0^{2\pi} A_{\mathbf{k}}^2 d\theta}{2\pi}$$
 (2)

This gives a 1D $\rho(k)$ function.

The resulting SDF plots can take various forms. Two examples of microstructures and their corresponding 1D SDF plots are shown in Fig. 2. The widely used two-point CRF is equivalent to inverse FT of SDF [58], but compared with two-point CRF, SDF is more convenient in differentiating spatial correlation features as evidenced in Fig. 2. Figures 2(a) and 2(b) represent two nanostructures with different structural properties. Figure 2(b) is an image of an ordered structure and has one distinctly strong correlation at a specific band of spatial frequency (Fig. 2(d)). This feature is also visible in the insets of Fig. 2(b) by a distinct circle in the Fourier spectrum. In contrast, Fig. 2(a) is less ordered, and hence, its SDF is more dispersed over the entire frequency spectrum (Fig. 2(c)). These differences in SDF based on structural changes corroborate the efficacy of SDF in capturing the structural detail. Furthermore, the SDFs observed in Figs. 2(c) and 2(d) both assume a simple shape that can be easily parametrized. The parametrized SDFs are represented as dashed lines in Figs. 2(c) and 2(d). For Fig. 2(c), it is a truncated Gaussian function, while for Fig. 2(d) it is a step function. Note that all the SDFs presented in this study are normalized for ease of comparison and consistency.

2.2 Spectral Density Function-Based Microstructure Design Framework for Organic Photovoltaic Cell Active Layer. Under the new paradigm of microstructure-sensitive material design [35,59], materials are viewed as a complex structural systems that can be optimized for achieving superior properties (properties under consideration are subject to targeted application). Using OPVC active layer optimization as an example, we present here a holistic SDF-based microstructure design framework (Fig. 3) that can be employed for design of quasi-random nano- or microstructural systems based on S–P relations.

The key idea of the proposed framework is to leverage SDF as the representation of OPVC microstructures, enabling direct and inverse S–P mappings. As shown in Fig. 3, the framework is initiated by fabricating samples of NMSs of interest (OPVC active layer for this article) using a nanofabrication technique with processing parameters choices based on empirical findings or literature. State-of-the-art imaging techniques are used to visualize the nanostructure in the available samples and the type (form) of SDF is identified. The main advantage of using SDF for quasi-random NMSs is that it can be easily parametrized (Sec. 2.1) and provides a more convenient representation for interpretation and design relative to other design methods [6]. Since SDF corresponds to the magnitude of FT of the microstructure, reconstruction can be cast as a phase recovery technique [60]. In this article, reconstruction is accomplished by level-cutting a Gaussian random field (GRF) governed by the required SDF. Thus, starting from a two-

Journal of Mechanical Design

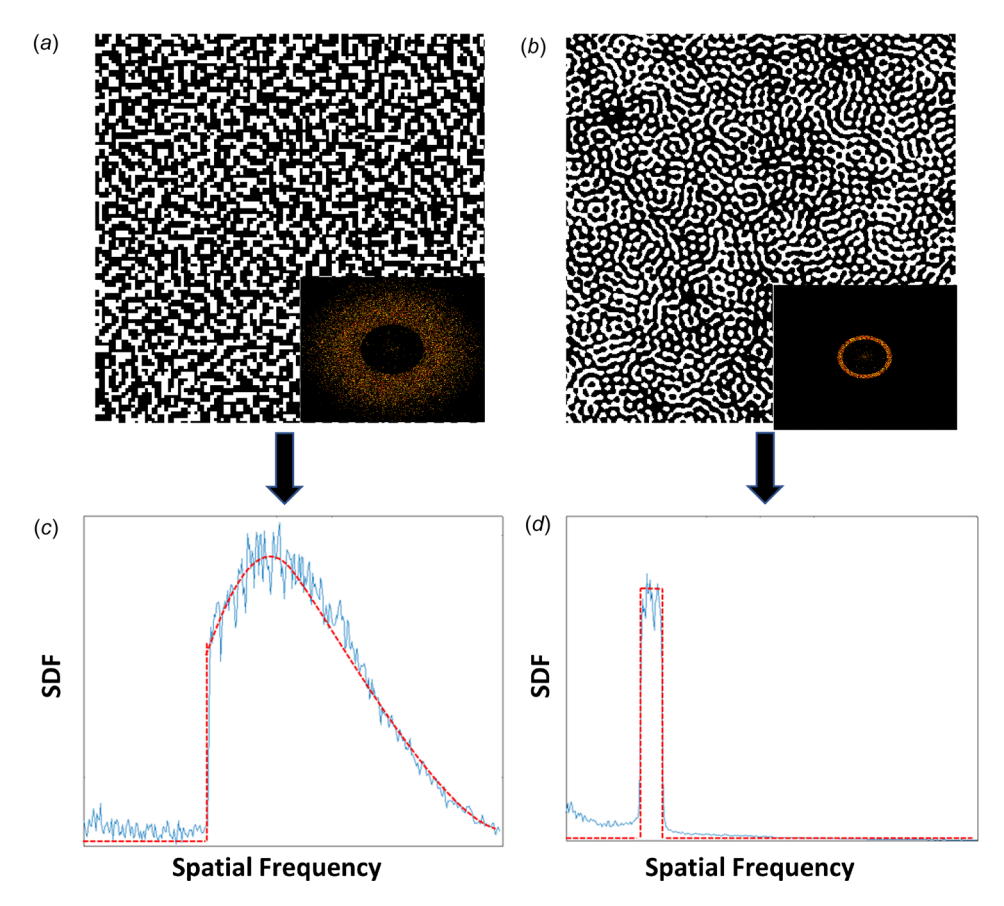


Fig. 2 Two sample microstructures (a) and (b) along with their Fourier spectrum in the insets; (c) and (d) are the final 1-D SDFs of each image. Dashed line represents the approximated SDF.

dimensional (2D) XSTM/S image, SDF provides a reduced-order microstructure representation (only three parameters required in this study) for creating statistically equivalent 3D microstructures which serve as representative volume element (RVE) for performance evaluation.

To evaluate the performance of a RVE, a model is sought that accounts for structural features in addition to device physics and material properties. For OPVCs, the key performance parameter of interest is the incident photon to converted electron (IPCE) ratio. To evaluate IPCE computationally, a novel strategy based

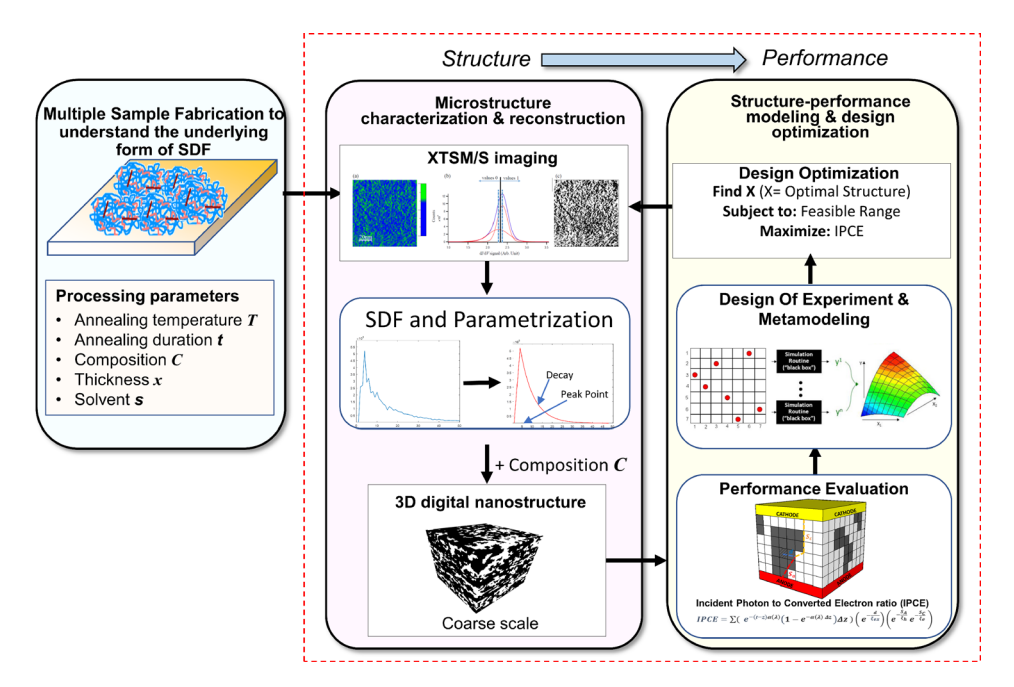


Fig. 3 A framework for designing active layer nanostructure in BHJ OPVC via SDF

111408-4 / Vol. 140, NOVEMBER 2018

on device physics and nanostructure is developed here. This strategy explicitly states the influence of nanostructure on known physical phenomena and establishes the S-P relationship that forms the basis for performance optimization. However, before the optimization, creating a metamodel to replace the computationally expensive and time-consuming S-P model is highly desirable (see Fig. 3). Metamodel, created by careful design of experiments (DOE), is essentially a "black-box" that approximates the S-P simulations. Given the set of design variables and their bounds, DOE dictates the S-P simulations that must be performed to determine the corresponding value of objective function (also known as response). A suitable machine learning model is chosen to interpolate between known values of response, forming a metamodel which can be queried at each iteration of the optimization. In this article, we use OLHS to create the metamodel based on the Kriging method, accelerating the search for the optimal

Design optimization is performed with the predetermined design variables obtained by parametrizing SDF (Sec. 4) along with the material composition. As mentioned previously, SDF provides a low-dimensional representation in reciprocal space of an otherwise high-dimensional nanostructure image, thereby facilitating a convenient design formulation. In this work, IPCE is chosen as the objective function with an aim of finding its maximum value and the corresponding SDF parameters (i.e., nanostructure). However, it should be noted that the optimum structure is limited to the same type of material system as the fabricated samples because the form of the SDF function used for optimization is determined based on the fabricated samples. In the following sections, we elaborate the procedure of implementing the proposed framework.

3 Sample Fabrication and Imaging

Fullerene-based acceptors, such as PCBM and PC70BM, have dominated the OPVC field for decades and achieved a decent PCE of 6.82% [61]. Recent developments with nonfullerene-based acceptors further push the PCE of OPVCs to \sim 13% [62,63]. Nevertheless, the BHJ quasi-random nanostructure in OPVC is still the dominating design for high PCE devices. Here, we focus on the most studied P3HT:PCBM acceptor/donor combination. The methodology and results presented here can be extended to all kinds of OPVCs with BHJ architecture.

There are five major parameters for fabricating BHJ active layers in OPVC devices: (1) P3HT/PCBM composition; (2) the solvent; (3) annealing temperature; (4) annealing duration; (5) thickness of the active layer (see Fig. 1). In this work, the parameter under focus is composition. Annealing temperatures and durations are chosen differently for the two cases (Table 1). Other processing parameters are kept the same.

P3HT (Solaris Chem, Inc., Saint-Lazare, QC, Canada) and PCBM (purity >99.5%, Solaris Chem, Inc.) are first prepared into separate 1.78 wt % precursor solutions with chlorobenzene (purity >99.5%, Sigma-Aldrich, St Louis, MO). Final solutions with desired P3HT:PCBM weight ratios of 1:1 and 2:1, are made by mixing the precursor solutions with corresponding amounts. The solutions were then spin coated onto the Si(100) substrate at \sim 1000 rpm for 1 min. The P3HT:PCBM/Si(100) is annealed at 100 °C for 20 min for the 1:1 sample, and at 150 °C for 5 min for the 2:1 sample, respectively. Table 1 summarizes these conditions for the two cases.

Scanning tunneling microscopy and spectroscopy (STM/S) is used to distinguish different organic molecules. More precisely,

Table 1 Summary of processing conditions of the two cases

	Case 1	Case 2
Weight ratio (P3HT:PCBM)	1:1	2:1
Annealing temperature and time	100°C for 20 min	150 °C for 5 min

the OPVC active layers are imaged with XSTM/S [64], which has also been successfully applied to OPVCs [65] and organometallic perovskites [66]. In the XSTM/S imaging, the sample is cut into desired shape and fractured in an ultra-high vacuum environment to ensure a contamination-free cross section surface is exposed for the STM measurement. Figure 4 shows a $100 \,\mathrm{nm} \times 100 \,\mathrm{nm} \,\mathrm{d}I/\mathrm{d}V$ mapping of P3HT:PCBM (case 2) sample. Based on the dI/dV point spectra, the green regions denote the P3HT-rich domains while the blue regions represent the PCBM-rich domains. Note that, here the brightness and contrast are arbitrarily chosen.

To consistently assign regions as P3HT-rich and PCBM-rich, the following procedure is employed. The dI/dV signal from Fig. 4(a) is first plotted into histogram, as illustrated in Fig. 4(b). This histogram cannot be fit by a single Gaussian function; rather two Gaussian peaks suitably represent the distribution, indicating that the data contains two main values, reflecting the two molecules, together with Gaussian noises. By determining the peak positions, one could further estimate a threshold to demarcate the two peak values. Then, 1 and 0 are assigned to each pixel, respectively, based on whether the dI/dV signal in each pixel is larger or smaller than the threshold. Using this procedure, we can systematically assign the domains for further analyses. The resulting binarized digital images of both cases are presented later in Fig. 5 (Sec. 4.1).

4 Active Layer Characterization and Reconstruction **Using Spectral Density Function**

This section examines the form of SDF for the two-dimensional STM images of the fabricated active layer samples. Further, an analytical reconstruction method based on level-cutting a Gaussian random field is implemented for constructing threedimensional RVEs, and the associated computational time is discussed.

4.1 Characterization. We attempt to characterize the images of the two cases, introduced in Sec. 3, acquired by the STM imaging technique and subsequent post-processing. Figures 5(a) and 5(b) show the binarized STM images for cases 1 and 2, respectively. The solid lines in Figs. 5(c) and 5(d), respectively, correspond to the SDFs of cases 1 and 2. Although the two SDFs have a unique peak point and the decay that follows, the underlying form remains the same. This observation suggests that the triangular type SDF is sufficient for the considered materials and the corresponding fabrication conditions. This form of SDF can be easily approximated by a function which is governed by two parameters: peak point and decay factor (which is a multiplication factor in the exponential decay following the peak). The dotted lines in Figs. 5(c) and 5(d) represent the approximated function that concurs with the original SDFs. These parameters constitute the design variables to be used for optimization and exploration purposes, as we can vary these variables to obtain different SDFs for reconstruction of the new designs of nanostructures.

To assess whether SDF sufficiently captures the complex microstructure morphology for the samples in this study, an example of validation test is presented here. Using the SDF of a 100 nm STM/S image of case 2, a 2D image was reconstructed. Some common CRFs of both the original and reconstructed image are shown in Fig. 6. In this figure, it is evident that SDF and twopoint CRF $(S_2(r))$ match well, while minor differences at higher order CRFs such as two-point cluster CRF ($C_2(r)$) and two-point lineal path function (L(r)), were observed. From design optimization perspective, such small discrepancies in the correlation function may not impact the optimal design solution as long as the design trend is captured correctly in structure-performance mapping.

4.2 Identifying Representative Volume Element Size. To

attain accuracy and minimize computational cost, it is essential

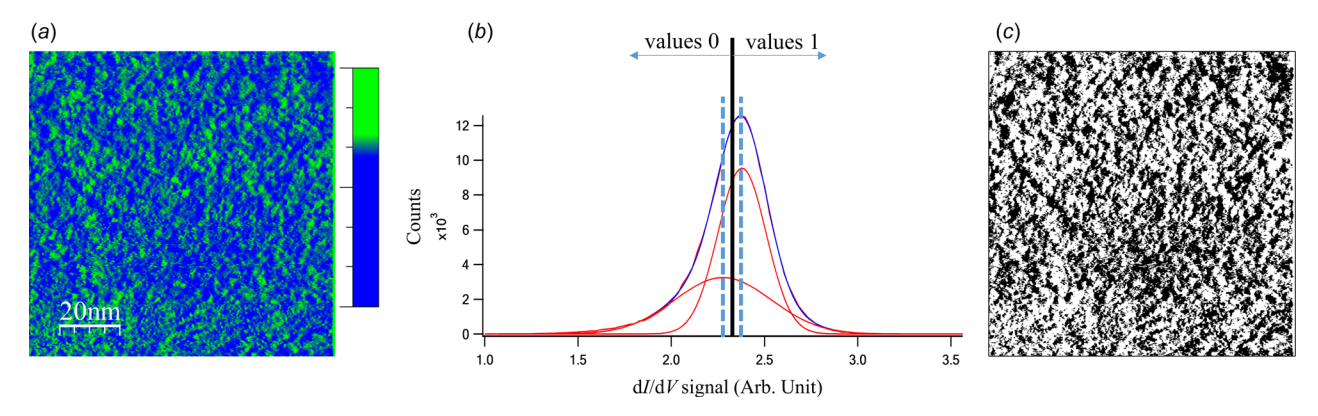


Fig. 4 (a) d/dV mapping of P3HT:PCBM active layer: $100 \text{ nm} \times 100 \text{ nm}$ scan size. Brightness and contrast are set arbitrarily. (b) Histogram fitted with two Gaussian functions. Dashed lines indicate the positions of the two Gaussian peaks. Solid line indicates the midpoint between the two Gaussian peak values. (c) Digital values (1 and 0) are assigned based on the d/dV values in each pixel compared to the solid line in (b).

that we determine the appropriate RVE size, for the material system of interest. We set two-point CRF as our property of interest to find the RVE size. We start with an STM image of $160\,\mathrm{nm} \times 160\,\mathrm{nm}$ and observe its two-point CRF. Then we reduce our window size so that we only observe 90% ($\sim 144\,\mathrm{nm}$) of the original image, and then calculate the two-point CRF. We continue narrowing the window of observation (decreasing 10% at a time) until the two-point CRF deviates significantly from the original image, as shown in Fig. 7. The Mean Absolute Percentage Error (MAPE) of the curves exceeds 10% if the size of the window goes below 60% (which is equal to $96\,\mathrm{nm}$). Hence, $100\,\mathrm{nm}$ is selected as the size of our RVE.

4.3 Microstructure Reconstruction Based on Spectral Density Function. Accurate structure-performance evaluations require digital 3D structures, so it is essential to generate 3D structures from the SDF in the most cost-effective way possible. The efficacy of using SDF for characterization has already been established in Sec. 4.1. In this section, the process of using SDF to create statistically equivalent 3D structures is elaborated.

Realizing the microstructure as a multi-variate sample taken from an underlying GRF [42], it can be concluded that the reconstruction of statistically equivalent microstructures can be achieved by finding that GRF. After finding the GRF, microstructures are reconstructed by taking realizations of these GRFs and

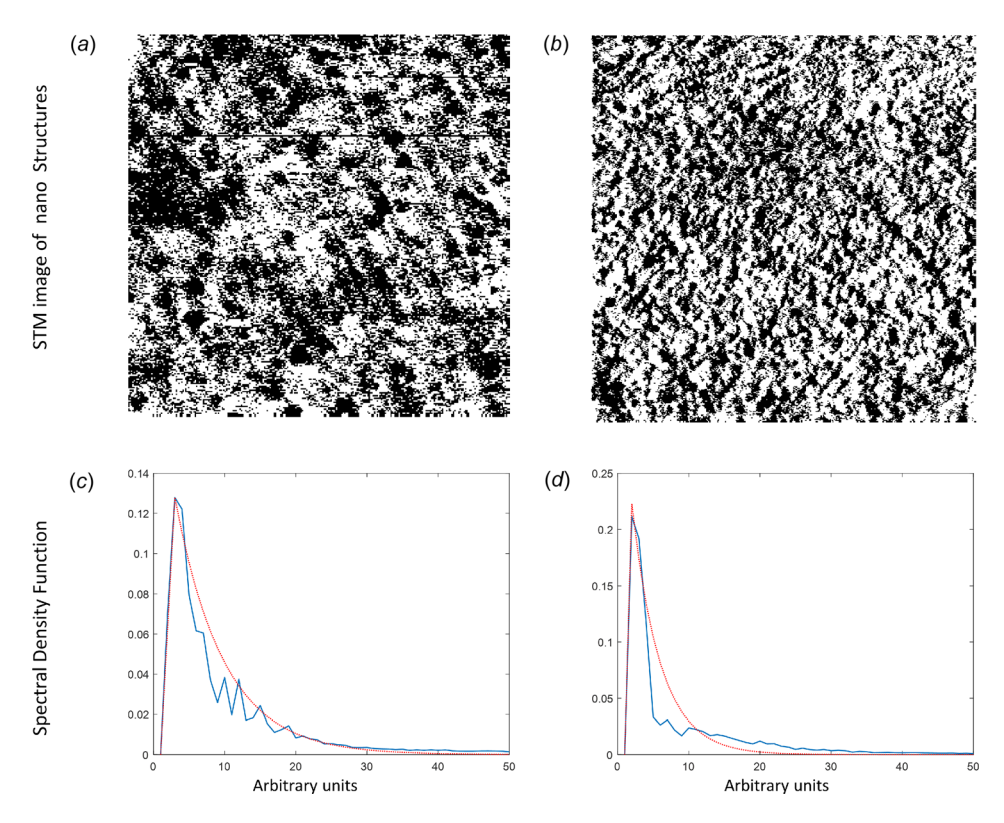


Fig. 5 Comparing SDF of the two cases mentioned in Table 1. (a) and (b) are binarized STM images of sizes $100 \text{ nm} \times 100 \text{ nm}$, for cases 1 and 2, respectively. (c) and (d) are the SDFs (solid line) of cases 1 and 2, respectively. In (c) and (d), the dotted line represent the approximations of the SDFs for each case.

111408-6 / Vol. 140, NOVEMBER 2018

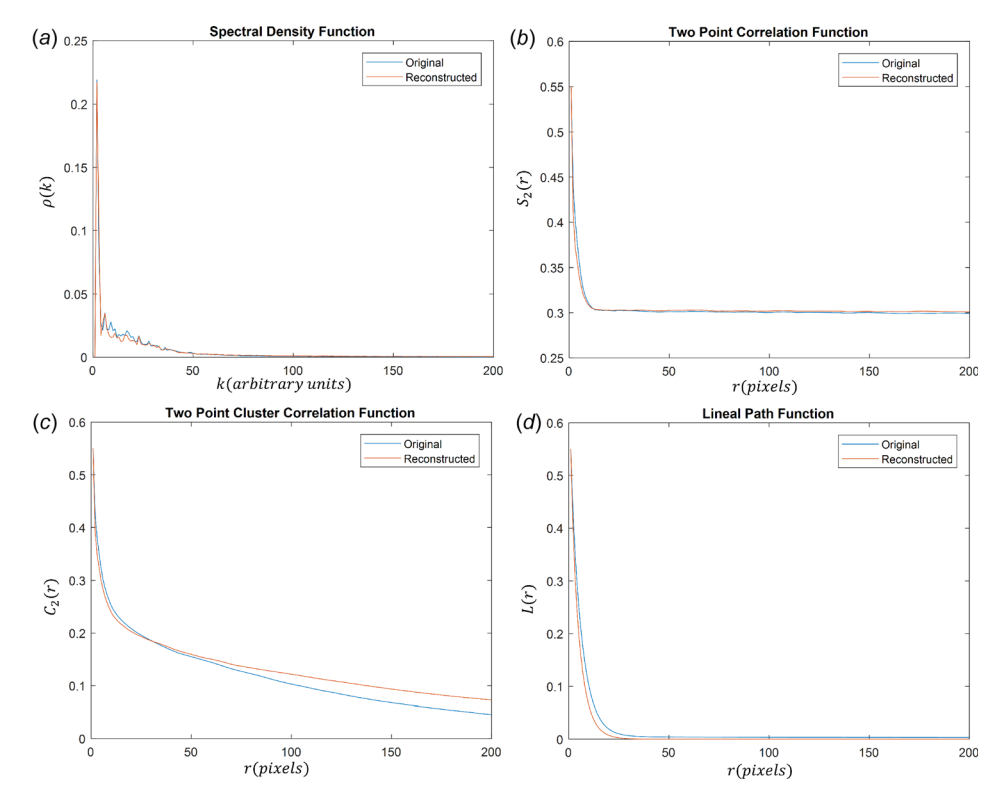


Fig. 6 Comparison of CRFs of an original image with a reconstructed image using SDF

then level cutting them based on a threshold which is the volume fraction (VF) of white phase in the original image.

For realizing the GRF, the Cahn's scheme [42] is utilized. It is an analytical approach for generating realizations from a GRF that has same SDF as the original microstructure. The governing equation is:

$$Y(\mathbf{r}) = \left(\frac{2}{N}\right)^{\frac{1}{2}} \sum_{i=1}^{N} \cos(k_i \hat{\mathbf{k}}_i \cdot \mathbf{r} + \emptyset_i)$$
 (3)

where $\hat{\mathbf{k}}_i$ and \emptyset_i are uniformly distributed on unit circle, and $[0,2\pi]$, respectively. k_i is a random variable whose probability density function, P(k), is determined by the SDF: $P(k) = \rho(k)k^2$ for a 3D GRF, and $\rho(k)k$ for a 2D GRF. After the generation of GRF, the final structure is extracted by carrying out a level cut based on the desired threshold. The number of samples N plays a critical role in the reconstruction. As we increase N, the statistical accuracy of the final image increases, but so does the computational cost. The result of the accuracy of reconstruction is shown in Fig. 8 along with the effects on consumption time. The reconstruction using $N=10^3$ and $N=10^4$ do not match either the height or peak point location on the x-axis. The reconstruction using $N=10^5$ captures the feature of the curve more accurately and identified to be the appropriate and affordable sampling size with a good degree of accuracy.

To check the robustness of the methodology, two realizations are produced of the STM image of case 1. SDF along with volume fraction is taken as input. Figure 9 quantitatively compares the two reconstructed SDFs with the SDF of the original image. For an enhanced pictorial representation of nanostructure, we reproduce the reconstructed image from one of the two realizations in Fig. 10. The reconstructed image qualitatively replicates the main characteristics of the original image.

Extending our tests to 3D, a cube of size $80 \times 80 \times 80$ pixel³ was created using an arbitrary SDF and volume fraction of 0.3. As seen in Fig. 11(a), the SDF of the reconstructed image matches well with that of the original. The 3D reconstructed structure is

shown in Fig. 11(b). Resolution of the structure can be improved by increasing the size of reconstruction, the tradeoff being an increase in the computational time. So, this size has been set as standard for optimization.

5 Structure-Performance Modeling Using an Analytical Equation

This section provides the details of a novel approach for finding the IPCE of a OPVC structure considering the microstructural features. The first half explains the physics-based theory behind the novel equation, while the second part lists down the assumptions along with presenting three test cases for the prevalidation of our approach.

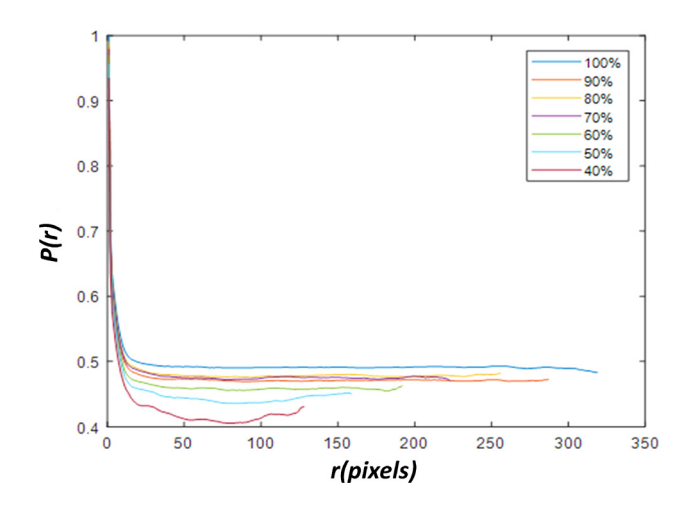


Fig. 7 Two-point CRF observed at different window sizes. The sizes of the windows vary from 100% (i.e., 160 nm) to 40% (i.e., 64 nm).

Journal of Mechanical Design

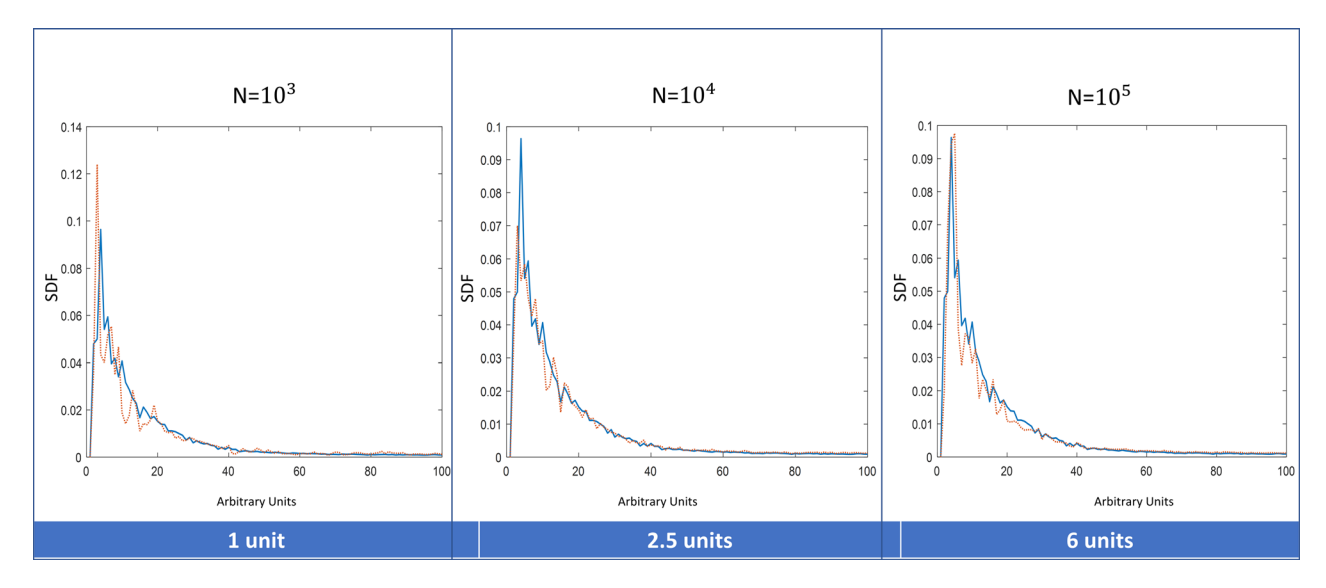


Fig. 8 The effect of increasing sampling on accuracy of reconstruction with the time consumed for reconstruction at the bottom. $N = 10^3$ is taken the reference, and the other two reconstruction times are in comparison to the first one.

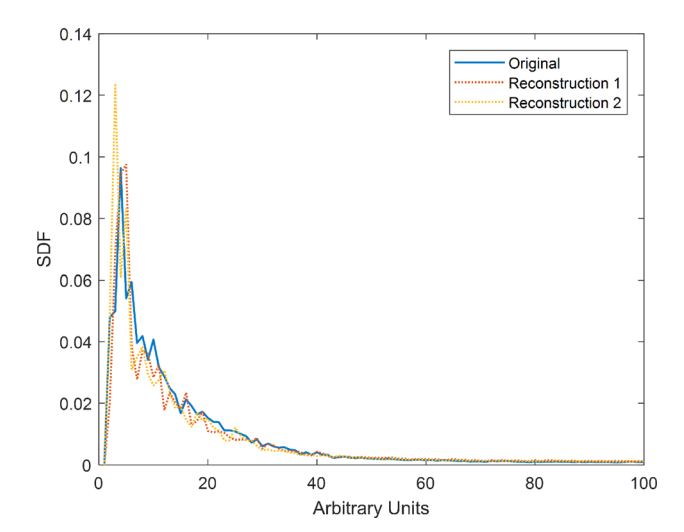


Fig. 9 SDF of original image along with two reconstructed images

5.1 Theory of Light to Electron Conversion Efficiency in an Organic Photovoltaic Cell. Here, a microscopic equation is developed for the first time to predict the device performance for a given 3D reconstructed microstructure. Under the finite element scheme, the equation for estimating performance from the microstructure can start with counting the number of collected electrons/holes per unit time through a summation of contributions from each volume element (voxel) over the whole active layer as

$$\frac{n(\lambda)}{\Delta t} = \sum \left(\frac{I(\lambda)}{h \frac{c}{\lambda}} e^{-(t-z)\alpha(\lambda)} \Delta x \Delta y P_{ex}(\lambda) \right) \\
\times \left(e^{-\frac{d}{\xi_{ex}}} \right) (P_{\text{sep}}) \left(e^{-\frac{S_A}{\xi_h}} e^{-\frac{S_C}{\xi_e}} P_{\text{col}} \right) \tag{4}$$

The four parentheses in Eq. (4) represent the four steps illustrated in Fig. 1: (i) light absorption (exciton creation); (ii) exciton diffusion; (iii) charge separation; (iv) charge diffusion and collection. Here, t is the thickness of the active layer; $\alpha(\lambda)$ is the absorption coefficient of active layer as function of the light wavelength, λ ; P refers to probability for exciton creation (ex), for charge separation (sep), and for charge collection (col); d is the distance to the

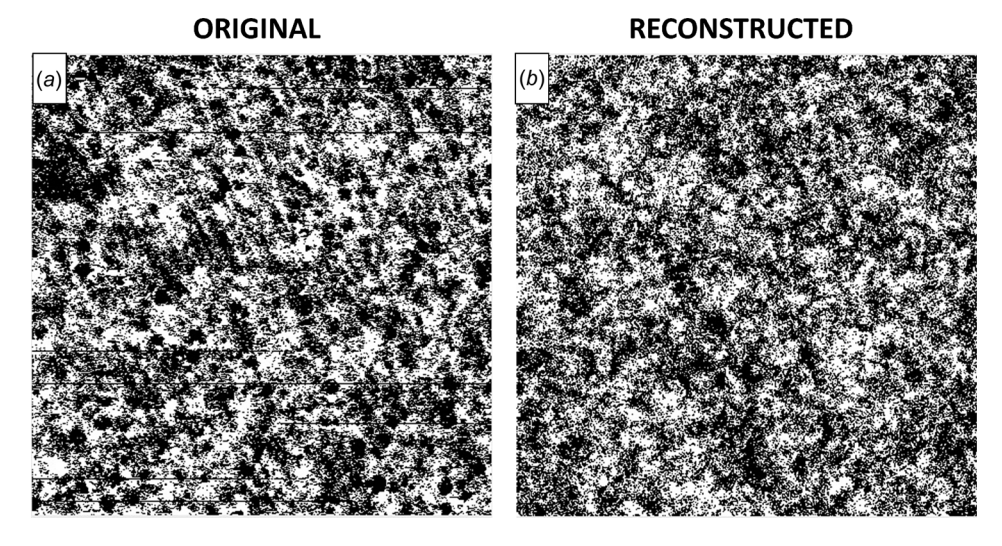


Fig. 10 (a) Initial image (of size 450 pixels \times 450 pixels) (b) Reconstructed (of size 450 pixels \times 450 pixels)

111408-8 / Vol. 140, NOVEMBER 2018

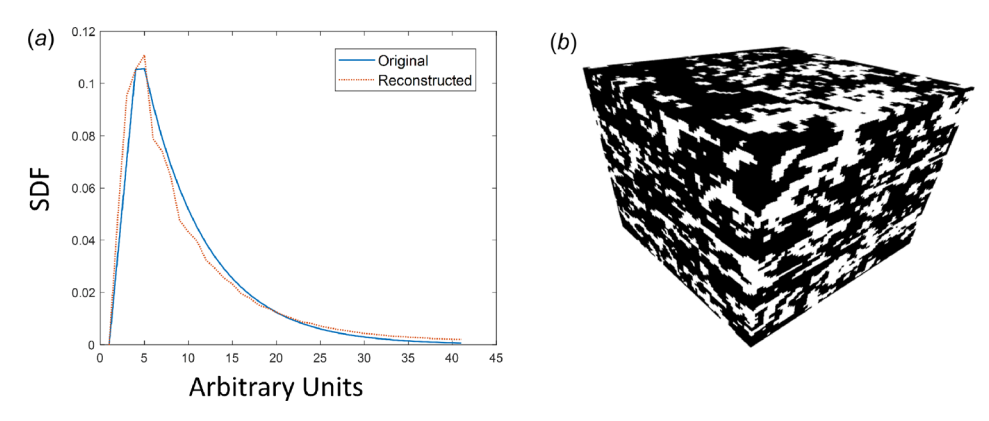


Fig. 11 (a) SDF of original image in comparison with the SDF of reconstructed 3D image/structure and (b) 3D realization of the reconstruction

nearest interface from the location of the exciton creation; ξ the diffusion lengths of exciton (ex); of hole (h); and of electron (e); S are the lengths of the path to anode (A); and to cathode (C). In this equation, the recombination behaviors of the charges are simply assumed to follow exponential decay over the distance it moves.

From previous study, the value of $\xi_{\rm e}$ (diffusion length for electron) is found to be $\sim\!340\,{\rm nm}$ [67]; value of $\xi_{\rm h}$ (diffusion length for hole) is found to be $\sim\!90\,{\rm nm}$ [67]; the value of $\xi_{\rm ex}$ (diffusion length for exciton) is found to be $5.4\!\pm\!0.7\,{\rm nm}$ [68] and $\alpha(\lambda)$ (absorption coefficient) is measured and could be found in Ref. [69].

Among the variables in Eq. (4), the probability of exciton creation, $P_{ex}(\lambda)$, and the absorption coefficient, $\alpha(\lambda)$, could be related to each other through the following relationship:

$$P_{ex} = 1 - e^{-\alpha(\lambda)\Delta z} \tag{5}$$

This relationship is deduced by assuming:

$$P_{ex}(\lambda) = \left(\frac{\text{no. of photon absorbed}}{\text{no. of photon incident}}\right) \cdot \left(\frac{\text{no. of exciton created}}{\text{no. of photon absorbed}}\right)$$

where the second term is closely related to the internal quantum efficiency, which is very close to 100% in many cases [70], so it is assumed to be 1 here. On the other hand, the first term is closely related to the photon absorption coefficient, $I(z) = I_0 e^{-\alpha(\lambda)z}$.

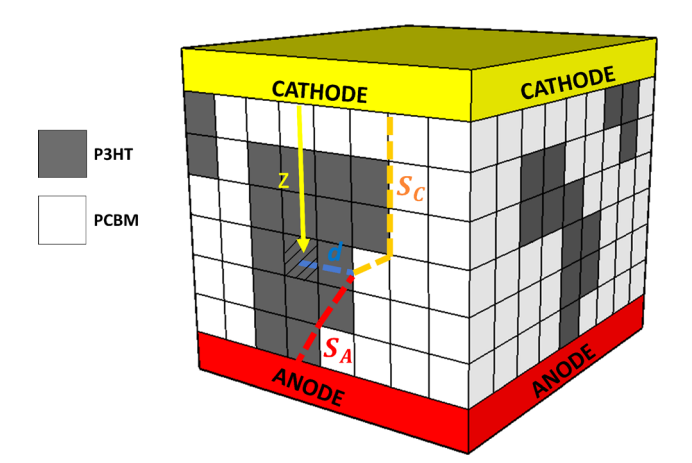


Fig. 12 A sample structure with an excited particle at the center (shaded cell). Yellow arrow represents light's path toward the prospective region; blue represents exciton's path; orange represents electron's path; red represents hole's path. For interpretation of the references to color in this figure legend, the reader is referred to the web version of this article.

Thus, Eq. (4) could be expressed as:

$$\frac{n(\lambda)}{\Delta t} = \sum \left(\frac{I(\lambda)}{h \frac{c}{\lambda}} e^{-(t-z)\alpha(\lambda)} \Delta x \Delta y \left(1 - e^{-\alpha(\lambda)\Delta z}\right) \right) \times \left(e^{-\frac{d}{\xi_{ex}}}\right) \left(P_{sep}\right) \left(e^{-\frac{S_A}{\xi_e}} P_{col}\right) \tag{7}$$

We compute the IPCE, which is the number of electrons collected per incident photon, as: $IPCE(\lambda) = n(\lambda)/\Delta t \ (1/(I(\lambda)/h\frac{c}{\lambda}))A$, where A represents the area of the sample illuminated by light. In this simulation, it is assumed that the whole sample surface is illuminated by light, indicating the sample surface area is A. The final working equation for evaluating IPCE from nanostructure is expressed as the summation over every voxel

IPCE(
$$\lambda$$
) = $\frac{1}{A}$... $\sum \left(\left(e^{-(t-z)\alpha(\lambda)} \Delta x \Delta y \left(1 - e^{-\alpha(\lambda)\Delta z} \right) \right) \times \left(e^{-\frac{d}{\xi_{ex}}} \right) \left(P_{\text{sep}} \right) \left(e^{-\frac{S_A}{\xi_h}} e^{-\frac{S_C}{\xi_e}} P_{\text{col}} \right) \right)$ (8)

where, z, d, S_A , and S_C of each voxel are determined from the nanostructure. Equation (8) is used to evaluate the performance of the OPVCs with the known quasi-random nanostructures in this study.

5.2 Three-Dimensional Structure Performance Simulation. To evaluate the IPCE for a 3D binary structure, some assumptions are made: (i) no void space exists in the structure—the whole space is filled by either one of the two materials: P3HT and PCBM; (ii) only P3HT is responsible for creating excitons upon light absorption. This condition is based on the fact that in the solar spectrum wavelength range, P3HT has 2–5 times larger absorption coefficient compared to PCBM. For simplification, both $P_{\rm sep}$ and $P_{\rm col}$ are set to 1 which being mere multiplication factors, will not affect the optimization. λ is chosen to be 510 nm, at which P3HT has the highest absorption coefficient $(\alpha(\lambda) = 4.3 \times 10^6 {\rm m}^{-1})$ [69]. Consideration of the whole wavelength range of solar spectrum can be easily implemented in the future.

Under these assumptions, there are four major parameters viz., z, d, S_A , and S_C at each voxel, required for optimizing the IPCE. In our 3D binary model, P3HT is assigned with 0s or black regions, while PCBM is assigned as 1s or white regions. Figure 12 illustrates these distances with an exciton created at the shaded cell and corresponding distances. First, excitons are created (step (1) in Fig. 1) at the shaded cell with the light intensity determined by the depth of this cell: t-z. After creation, the exciton diffuses to the nearest interface (step (2) in Fig. 1) with a distance d. When

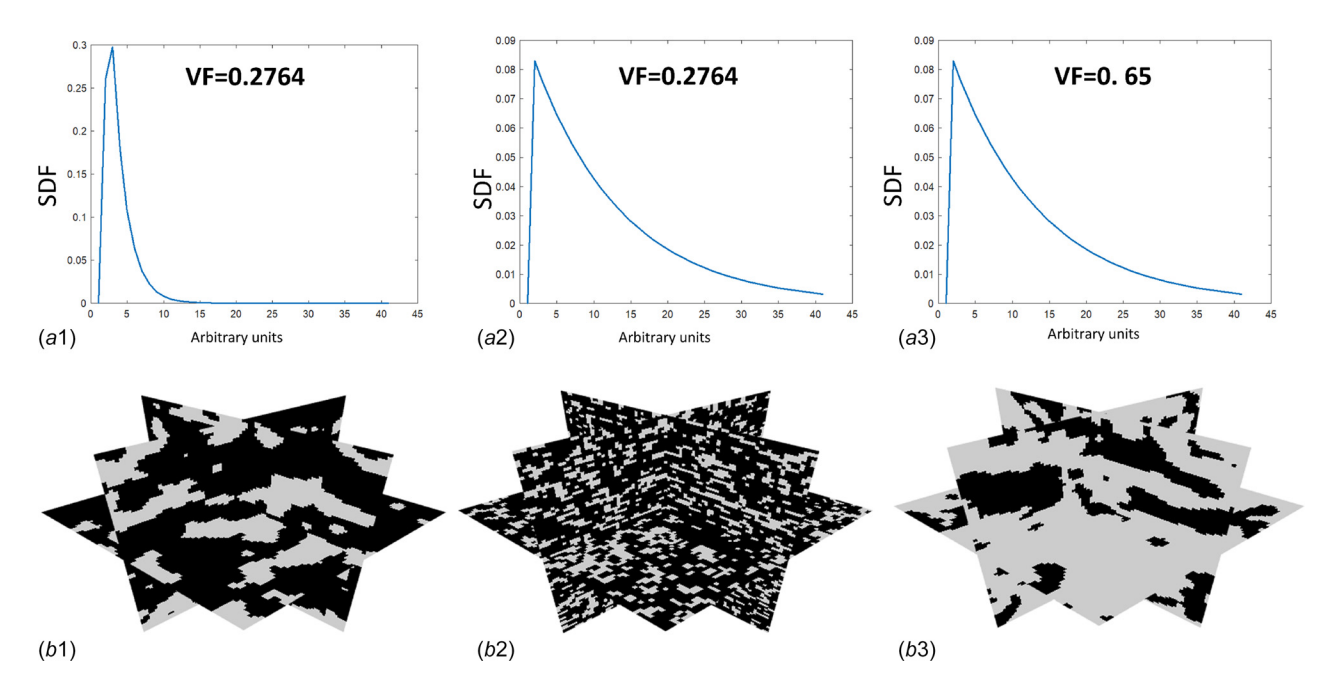


Fig. 13 Testing our performance model. (a1-a3) are input parameters: SDF and volume fraction; (b1-b3) are random cross-sectional slices of the reconstructed structure.

the exciton dissociates into electron and hole at the interface (step (3) in Fig. 1), the hole diffuses toward the anode through the shortest path in the black medium (step (4) in Fig. 1), S_A , while the electron diffuses toward cathode through the shortest path in the white medium (step (4) in the Fig. 1), S_C .

To explain the contribution of each of the three factors, peak point, decay, and VF, we randomly created three test structures for a basic preliminary verification of our model. The input parameters along with the cross-sectional slices of the resulting structure are shown in Fig. 13. The performance results are broken down in Table 2. As seen in the table, tests 1 and 2 have same VF, but different IPCE. This is because of the difference in the dispersion of the material which is caused by the different SDFs. The SDF in the test 1 has faster decay rate, thus, test 1 has larger clusters in real space; while the SDF in the test 2 has slower decay rate, leading to smaller clusters in real space. This results in larger average d and S_C in test 1 than that in test 2. With the same VF, the exciton creation is in the same order in the two test cases, thus the higher IPCE found in test 2 is attributed to the shorter average diffusion lengths, as shown in Eq. (8). On the other hand, comparing tests 2 and 3, which have the same SDF but different VF, the difference in VF dominates the IPCE value. With similar microstructure texture due to the same SDF input, test 2 has higher amount of P3HT molecules (lower VF), hence higher IPCE. It is worth noting that even tests 2 and 3 have same SDF input, their average diffusion lengths are affected by the VF. Thus, simultaneously optimizing the IPCE with consideration of both SDF and VF is critical and will be discussed in Sec. 7.

Table 2 Average values of d, S_A , and S_C are tabulated for the three cases presented in Fig. 13. Exciton generated is the number of P3HT voxels in the structure that will contribute toward performance.

	Test 1	Test 2	Test 3
Average d	4.3	1.77 nm	2.76 nm
Excitons generated	370,483	370,483	179,200
Average S_A	61.6 nm	60.4 nm	80.5 nm
Average S_c	96.0 nm	82.5 nm	65.2 nm
IPCE	4.97%	8.41%	3.04%

6 Design Formulation and Metamodeling

With the S–P relationship established through IPCE (Eq. (8)), design formulation can be cast as an optimization problem to find the active layer nanostructure that delivers highest IPCE. Due to the short exciton diffusion length (\sim 10 nm), the state-of-the-art OPVC nanostructure follows the BHJ architecture with the electron donor and acceptor domains in \sim 10 nm scale in the active layer. Ideally, to have all four major charge carrier processes optimized, the nanostructures in BHJ should possess the following characteristics: (a) thickness identical to the light absorption depth (typically approximately hundreds of namometers to a micron), to best utilize the light flux; (b) the length scale of the nanostructures is of the order of the exciton mean free path (\sim 10 nm); (c) maximizing effective interfacial charge separation volumes for efficient charge separation; (d) minimizing the isolated domains where there is no path to electrodes for charge collection.

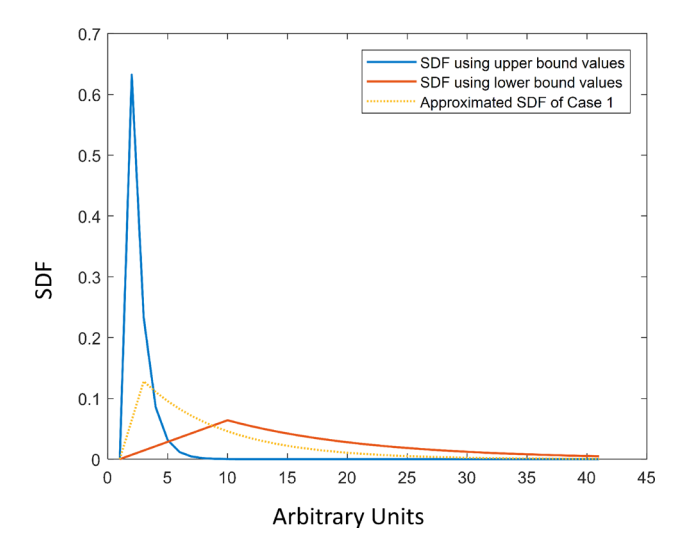


Fig. 14 SDF curves are plotted using the upper bounds and lower bounds of design variables of SDF. SDF of case 1 is also plotted for reference.

We leverage the low-dimensional structure representation enabled by SDF to formulate a design paradigm using a small set of variables. The active layer thickness is determined by the size of RVE, 100 nm (Sec. 4.2), while the SDF parameters—peak point and decay—account for structural characteristics that control the charge separation and transport phenomenon discussed above. Further, the assumption that exciton generation is restricted to P3HT molecules necessitates the inclusion of donor/acceptor composition as an additional design variable. Here, PCBM volume fraction is chosen as the composition design variable. Note that composition also plays a critical role in level cutting the GRF for the reconstruction. Thus, only three variables are required: two from SDF plus the PCBM volume fraction.

The bounds for design variables are selected by analyzing the SDF of the two fabricated samples (Table 1) to estimate the three SDF parameters. Then, a broad range for each of the three parameters is selected to ensure diverse SDF curves. Figure 14 plots the SDF obtained by setting parameters to their lower and upper bounds, along with the SDF of case 1 for comparison. Previous studies, focusing only on active layer composition, have revealed that the ideal PCBM VF is 0.37 approximately [25,71]. To explore a wider range of values around the optimum, we allow VF to vary between 0.15 and 0.75. With the objective of maximizing IPCE ratio, the optimization problem can be stated as

$$\begin{array}{ll} \max & \text{IPCE} = f(p,d,vf) \\ \text{with respect to} & p,d,vf \\ \text{s.t.} & 2 \leq p \leq 10 \\ & 1 \leq d \leq 12 \\ & 0.15 \leq vf \leq 0.75 \end{array} \tag{9}$$

where p = peak point, d = decay, and vf = volume fraction.

Since optimization is an iterative process, it requires several S–P simulations (constructing RVE for current value of design variables and evaluating the IPCE ratio). For an $80\times80\times80$ voxels RVE, reconstruction requires several minutes, implying that one iteration will need the same time. To overcome this computational burden and accelerate optimization, a metamodel is used.

A metamodel is created by sampling design space efficiently using DOE, followed by an appropriate machine learning method to interpolate and form a continuous input-output mapping in design space. One of the main hurdles in choosing sampling points is to ensure that the design space is thoroughly explored with the minimum number of samples. For the selection of these sampling points, we use OLHS. The main advantages of OLHS include minimization of integrated mean square error, maximization of minimum distances between samples, and maximizing entropy [72]. Since there are three design variables, 56 space filling samples are obtained from OLHS and corresponding S-P simulations were performed. The machine learning technique used to create the metamodel is Gaussian process (GP), which is a special case of Kriging method. The main advantage of using Kriging method is that it provides the most accurate results for highly nonlinear models with small number of variables compared to polynomial regression, radial basis function or multivariate adaptive regression splines [73]. Over 45 randomly selected samples are used in creating the metamodel while 11 are used for crossvalidation.

7 Design Optimization and Sensitivity Analysis

This section discusses the use of the two DOE models for understanding the effect of design variables on the design performance, i.e., IPCE. In the first model (Sec. 7.1), all design variables—peak point, decay, and VF are included. Global sensitivity analysis using this model reveals the effects of all the variables on performance. In the second model, the material composition (volume fraction) is fixed, and the metamodel is

Table 3 Sobol indices for all design variables

	Peak point	Decay	VF
S_i (MAIN effect)	0.0033	0.1426	0.8253
S_{Ti} (TOTAL effect)	0.0116	0.17010	0.8479

created over three SDF parameters as inputs to closely examine the effects of material morphology on performance. Optimal design of the microstructure is obtained subsequently using the metamodel.

7.1 Effect of All Design Variables on Incident Photon to Converted Electron Ratio and the Optimal Design. As mentioned in Sec. 6, 45 randomly selected samples from OLHS design were used for creating the Kriging metamodel with all four design variables while 11 were used for cross-validation. The R-squared value based on validation points is 0.9792, which indicates a fair fit. Because of the highly nonlinear response of the metamodel, genetic algorithm (GA) is applied to obtain the global maximum IPCE. To test accuracy, multiple starting designs were selected. For all starting points considered in this study, the optimization routine converges to the same optimal point (peak point = 2, decay = 12, VF = 0.2764 and IPCE = 8.41%). This result relates to a 36.75% increase in IPCE ratio compared to case 1 which has an IPCE ratio of 6.15%. A RVE is reconstructed using the optimal microstructure design variables and its IPCE ratio is computed. Compared to 8.41% from the metamodel, the reconstructed RVE results in an IPCE ratio of 8.19%, reinforcing the fact that the metamodel used here is sufficiently accurate.

Next, we analyze the effect of each variable in the performance model using the variance-based sensitivity analysis (also known as Sobol analysis [56]). This analysis consists of two indices for each variable i: first-order sensitivity (S_i), and total-order sensitivity (S_{Ti}). S_i essentially incorporates the effect of variable x_i alone on the response while S_{ij} incorporates the total effect of variable x_i , including the interaction effect with other variables [56]. The Sobol indices for all three design variables are listed in Table 3. We note that VF is the most influential design variable as it has the greatest first-order and total effect. Similar conclusions can also be deduced by plotting the variation of IPCE ratio with respect to decay and VF (see Fig. 15). It further confirms the optimal value of VF (0.2764), which translates to a composition of P3HT:PCBM = 1.92:1 (using densities of P3HT and PCBM as 1.1 g/cm^3 and 1.5 g/cm^3 , respectively [74]).

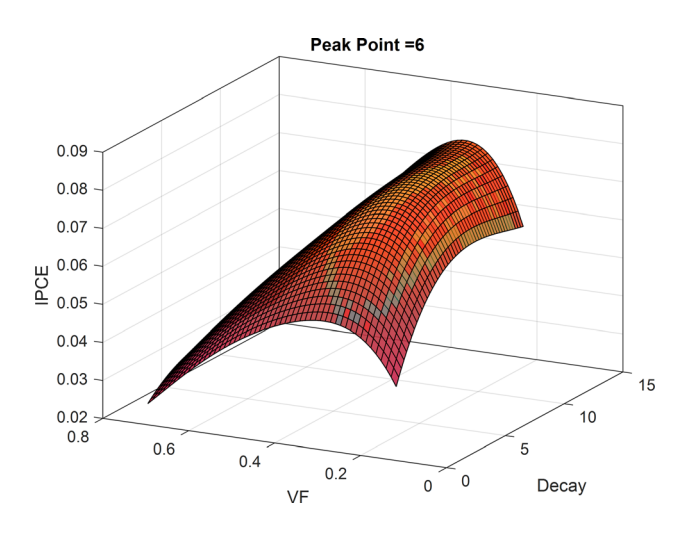


Fig. 15 The effect of VF and decay on performance with peak point fixed

Journal of Mechanical Design

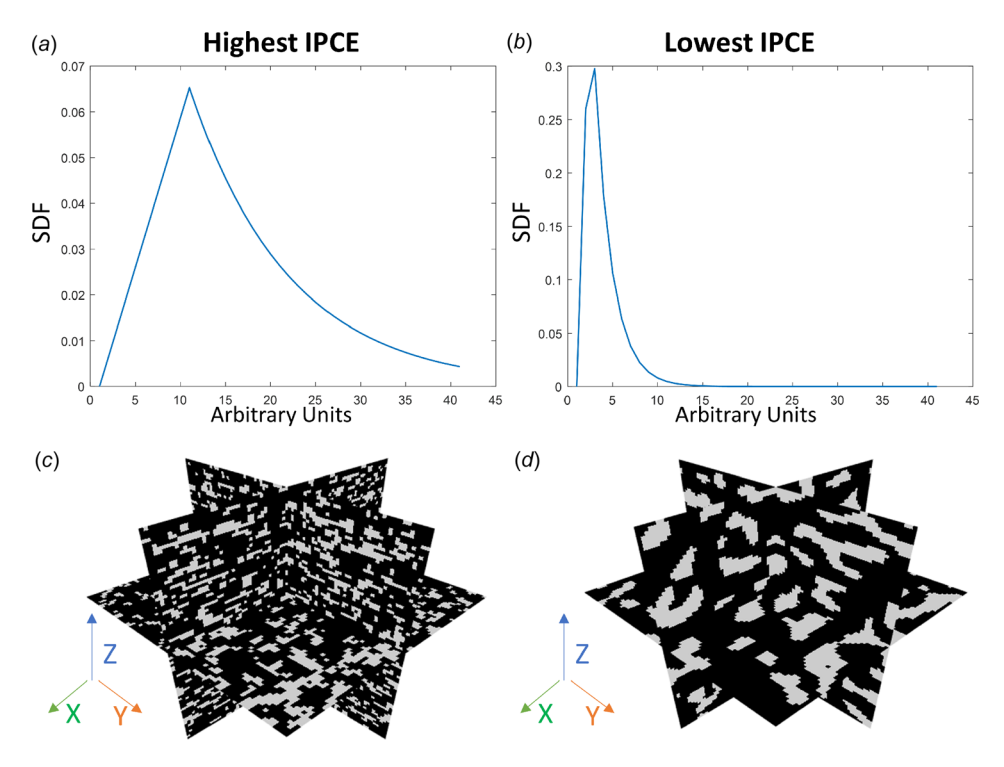


Fig. 16 The SDF and 3D slices of nanostructures with highest (a) and (c) and lowest (b) and (d) IPCE ratio. White regions comprise PCBM while black regions are occupied by P3HT.

7.2 Effect of Spectral Density Function on Incident Photon to Converted Electron Ratio and the Optimal Design. To get a deeper understanding on the effects of two SDF parameters on OPVC performance, we constrain the VF to 0.2764 and create a metamodel using only the two SDF parameters—peak point and decay. We maintain the range of these variables as mentioned in Eq. (9) for comparison. OLHS is used to obtain 30 samples for creating the metamodel using the Kriging technique and six for validation. The *R*-squared value for this model is 0.973, which suggests a good fit.

Optimization is run with different starting designs and all cases converge to the optimal IPCE value of 8.24% at (peak point = 10, and decay = 11.05). A RVE reconstructed with optimal SDF parameters leads to IPCE ratio of 8.27%, showing good agreement with the value obtained from the metamodel as well as the optimal IPCE ratio obtained in Sec. 7.1. The maximum and minimum IPCE ratio observed in the samples for creating the metamodel is 8.24% and 3.68%, respectively. This demonstrates that for VF fixed at 0.2764, IPCE ratio can be varied as much as 120% by varying the SDF parameters within the bounds indicated in Eq. (9). We plot the SDFs and nanostructures corresponding to the two limiting cases described above in Fig. 16. As seen in the Fig. 16(c) with the largest IPCE ratio (best design), PCBM is distributed more evenly compared to the large agglomerations in nanostructure with the lowest IPCE ratio shown in Fig. 16(d). The uniform distribution of PCBM reduces the distance traveled by exciton toward the nearest donor/acceptor interface, d. Lower the distance d, greater the IPCE as evident from Eq. (8). Uniform distribution of PCBM also creates paths for the holes and electrons to reach the anode and cathode using P3HT and PCBM, respectively. However, for the nanostructure with lowest IPCE (Fig. 16(d)), there is high probability that holes and electron may not be able to reach the anode or cathode due to a lack of contiguous path in either media.

8 Conclusion and Future Work

This article introduced an SDF based microstructure design framework to accelerate the development of quasi-random NMSs.

Instead of following the conventional trial-and-error approach to materials design, the proposed framework enables physics-based, cost-effective design strategy by leveraging physics-aware SDF, a MCR technique capable of representing arbitrary geometries whose distribution is governed by an underlying spatial correlation. The focus of this paper is on implementing the proposed framework for the active layer design in OPVC. Active layer samples conforming to BHJ architecture are fabricated using spincoating technique, followed by annealing and their microstructure is captured by novel XSTM/S technique. By using SDF to represent these microstructural images, we confirm that the nanostructure in the OPVC active layer can be parametrized using the SDF with only two variables—peak point and decay, providing a lowdimensional representation of an otherwise infinite-dimensional microstructural image. Accurate 3D RVEs are obtained by levelcutting GRFs and the associated computational cost for different sample sizes is discussed. A novel S-P simulation model is developed using the IPCE ratio as the metric to evaluate OPVC performance computationally. In addition to accounting for the physical processes and material properties influencing energy conversion as already established in literature, our proposed IPCE evaluation takes the impact of active layer morphology explicitly into account and delineates its effects on each physical process. The distance to nearest donor/acceptor interface (d), shortest path to anode (S_A) and cathode (S_C) are the three morphological variables influencing IPCE. Procedure to evaluate these variables is discussed, followed by IPCE computation to establish S-P linkage. Our results also demonstrate the effectiveness of using SDF for design representation and the use of computationally guided methods to expedite microstructural design optimization involving expensive S–P simulations. A metamodel created using OLHS and Kriging method is used to accelerate the iterative optimization problem, which is formulated with the objective of maximizing IPCE using only three design variables—two from SDF plus the PCBM volume fraction. The optimal microstructure has an IPCE of 8.41%, a 36.75% increase compared to fabricated sample (case 1). Global sensitivity analysis using Sobol indices shows that PCBM volume fraction is the most influential design variable followed by Decay (which controls the dispersion of PCBM).

111408-12 / Vol. 140, NOVEMBER 2018

Future work will involve establishing P–S linkage, which necessitates coarse-grained molecular dynamics simulations for microscopic examination of morphology and construction of atomic-resolution structural realizations of interfaces and molecular alignment. A wider range of fabrication techniques and processing conditions will be explored and the corresponding forms of SDF will be identified. With the help of coarse-grained molecular dynamics for studying processing–structure relations, the processing–structure–property linkages will be established, and a goal-oriented design methodology will enable optimizing OPVC performance with due consideration of the necessary processing conditions, thus ensuring manufacturing feasibility of the optimized nanostructures. Finally, the optimal nanostructure will be fabricated using a suitable bottom-up nanofabrication technique and its performance will be validated experimentally.

Funding Data

- National Science Foundation (NSF) (Grant Nos. CMMI-1662435, 1662509, and 1753770).
- The Design of Engineering Material Systems (DEMS) program NSF EEC 1530734.

References

- Gleiter, H., 2000, "Nanostructured Materials: Basic Concepts and Microstructure." Acta Mater. 48(1), pp. 1–29.
- structure," Acta Mater., 48(1), pp. 1–29.
 [2] Lee, W. K., Yu, S., Engel, C. J., Reese, T., Rhee, D., Chen, W., and Odom, T. W., 2017, "Concurrent Design of Quasi-Random Photonic Nanostructures," Proc. Natl. Acad. Sci. U.S.A., 114(33), pp. 8734–8739.
- [3] Wang, C., Yu, S., Chen, W., and Sun, C., 2013, "Highly Efficient Light-Trapping Structure Design Inspired by Natural Evolution," Sci. Rep., 3(1), p. 1025.
- [4] Yu, S., Wang, C., Sun, C., and Chen, W., 2014, "Topology Optimization for Light-Trapping Structure in Solar Cells," Struct. Multidiscip. Optim., 50(3), pp. 367–382.
- [5] Yu, S., Wang, C., Zhang, Y., Dong, B., Jiang, Z., Chen, X., Chen, W., and Sun, C., 2017, "Design of Non-Deterministic Quasi-Random Nanophotonic Structures Using Fourier Space Representations," Sci. Rep., 7(1), p. 3752.
- [6] Yu, S., Zhang, Y., Wang, C., Lee, W. K., Dong, B., Odom, T. W., Sun, C., and Chen, W., 2017, "Characterization and Design of Functional Quasi-Random Nanostructured Materials Using Spectral Density Function," ASME J. Mech. Des., 139(7), p. 071401.
- [7] Sanchis, L., Håkansson, A., López-Zanón, D., Bravo-Abad, J., and Sánchez-Dehesa, J., 2004, "Integrated Optical Devices Design by Genetic Algorithm," Appl. Phys. Lett., 84(22), pp. 4460–4462.
- [8] Gondarenko, A., Preble, S., Robinson, J., Chen, L., Lipson, H., and Lipson, M., 2006, "Spontaneous Emergence of Periodic Patterns in a Biologically Inspired Simulation of Photonic Structures," Phys. Rev. Lett., 96(14), p. 143904.
- [9] Jensen, J. S., and Sigmund, O., 2011, "Topology Optimization for Nano-Photonics," Laser Photonics Rev., 5(2), pp. 308–321.
 [10] Imboden, M., and Bishop, D., 2014, "Top-down Nanomanufacturing," Phys.
- [10] Imboden, M., and Bishop, D., 2014, "Top-down Nanomanufacturing," Phys Today, 67(12), pp. 45–50.
- [11] Kinoshita, S., Yoshioka, S., and Miyazaki, J., 2008, "Physics of Structural Colors," Rep. Prog. Phys., 71(7), p. 076401.
- [12] Vukusic, P., and Sambles, J. R., 2003, "Photonic Structures in Biology," Nature, 424(6950), p. 852.
- [13] Dufresne, E. R., Noh, H., Saranathan, V., Mochrie, S. G., Cao, H., and Prum, R. O., 2009, "Self-Assembly of Amorphous Biophotonic Nanostructures by Phase Separation," Soft Matter, 5(9), pp. 1792–1795.
- [14] Dong, B. Q., Zhan, T. R., Liu, X. H., Jiang, L. P., Liu, F., Hu, X. H., and Zi, J., 2011, "Optical Response of a Disordered Bicontinuous Macroporous Structure in the Longhorn Beetle Sphingnotus Mirabilis," Phys. Rev. E, 84(1), p. 011915
- [15] Walker, B., Tamayo, A. B., Dang, X. D., Zalar, P., Seo, J. H., Garcia, A., Tanti-wiwat, M., and Nguyen, T. Q., 2009, "Nanoscale Phase Separation and High Photovoltaic Efficiency in Solution-Processed, Small-Molecule Bulk Heterojunction Solar Cells," Adv. Funct. Mater., 19(19), pp. 3063–3069.
- [16] Peet, J., Heeger, A. J., and Bazan, G. C., 2009, "Plastic Solar Cells: Self-Assembly of Bulk Heterojunction Nanomaterials by Spontaneous Phase Separation," Acc. Chem. Res., 42(11), pp. 1700–1708.
- [17] Lee, W.-K., Jung, W.-B., Nagel, S. R., and Odom, T. W., 2016, "Stretchable Superhydrophobicity From Monolithic, Three-Dimensional Hierarchical Wrinkles," Nano Lett., 16(6), pp. 3774–3779.
- [18] Zhang, Y., Dong, B., Chen, A., Liu, X., Shi, L., and Zi, J., 2015, "Using Cuttle-fish Ink as an Additive to Produce Non-Iridescent Structural Colors of High Color Visibility," Adv. Mater., 27(32), pp. 4719–4724.
- [19] Biswas, A., Bayer, I. S., Biris, A. S., Wang, T., Dervishi, E., and Faupel, F., 2012, "Advances in Top-down and Bottom-Up Surface Nanofabrication:

- Techniques, Applications and Future Prospects," Adv. Colloid Interface Sci., 170(1-2), pp. 2-27.
- [20] Brabec, C., Scherf, U., and Dyakonov, V., 2011, Organic Photovoltaics: Materials, Device Physics, and Manufacturing Technologies, Wiley, Hoboken, NI
- [21] Brabec, C. J., 2004, "Organic Photovoltaics: Technology and Market," Sol. Energy Mater. Sol. Cells, 83(2–3), pp. 273–292.
- [22] Kippelen, B., and Brédas, J.-L., 2009, "Organic Photovoltaics," Energy Environ. Sci., 2(3), pp. 251–261.
- [23] Brabec, C. J., Dyakonov, V., Parisi, J., and Sariciftci, N. S., 2013, Organic Photovoltaics: Concepts and Realization, Springer Science & Business Media, New York.
- [24] Heeger, A. J., 2001, "Nobel Lecture: Semiconducting and Metallic Polymers: The Fourth Generation of Polymeric Materials," Rev. Mod. Phys., 73(3), p. 681
- [25] Berger, P., and Kim, M., 2018, "Polymer Solar Cells: P3HT:PCBM and Beyond," J. Renewable Sustainable Energy, 10(1), p. 013508.
- [26] Grancini, G., Polli, D., Fazzi, D., Cabanillas-Gonzalez, J., Cerullo, G., and Lanzani, G., 2011, "Transient Absorption Imaging of P3HT:PCBM Photovoltaic Blend: Evidence for Interfacial Charge Transfer State," J. Phys. Chem. Lett., 2(9), pp. 1099–1105.
- [27] Dang, M. T., Hirsch, L., and Wantz, G., 2011, "P3HT:PCBM, Best Seller in Polymer Photovoltaic Research," Adv. Mater., 23(31), pp. 3597–3602.
- [28] McDowell, D. L., Panchal, J., Choi, H.-J., Seepersad, C., Allen, J., and Mistree, F., 2009, Integrated Design of Multiscale, Multifunctional Materials and Products, Butterworth-Heinemann, Oxford, UK.
- [29] Mistree, F., 2002, "Robust Concept Exploration Methods in Materials Design," Ninth AIAA/ISSMO Symposium on Multidisciplinary Analysis and Optimization, p. 5568.
- [30] Olson, G. B., 1997, "Computational Design of Hierarchically Structured Materials," Science, 277(5330), pp. 1237–1242.
- [31] Matthews, J., Klatt, T., Morris, C., Seepersad, C. C., Haberman, M., and Shahan, D., 2016, "Hierarchical Design of Negative Stiffness Metamaterials Using a Bayesian Network Classifier," ASME J. Mech. Des., 138(4), p. 041404.
 [32] Liu, K., Detwiler, D., and Tovar, A., 2017, "Optimal Design of Nonlinear Mul-
- [32] Liu, K., Detwiler, D., and Tovar, A., 2017, "Optimal Design of Nonlinear Multimaterial Structures for Crashworthiness Using Cluster Analysis," ASME J. Mech. Des., 139(10), p. 101401.
- [33] Seepersad, C. C., Allen, J. K., McDowell, D. L., and Mistree, F., 2006, "Robust Design of Cellular Materials With Topological and Dimensional Imperfections," ASME J. Mech. Des., 128(6), pp. 1285–1297.
- [34] McDowell, D. L., and Olson, G., 2008, "Concurrent Design of Hierarchical Materials and Structures," Sci. Model. Simul., Springer, 15(1), pp. 207–240.
- [35] Fullwood, D. T., Niezgoda, S. R., Adams, B. L., and Kalidindi, S. R., 2010, "Microstructure Sensitive Design for Performance Optimization," Prog. Mater. Sci., 55(6), pp. 477–562.
- [36] Sopu, D., Soyarslan, C., Sarac, B., Bargmann, S., Stoica, M., and Eckert, J., 2016, "Structure-Property Relationships in Nanoporous Metallic Glasses," Acta Mater., 106, pp. 199–207.
- [37] Gupta, A., Cecen, A., Goyal, S., Singh, A. K., and Kalidindi, S. R., 2015, "Structure–Property Linkages Using a Data Science Approach: Application to a Non-Metallic Inclusion/Steel Composite System," Acta Mater., 91, pp. 239–254.
- [38] Çeçen, A., Fast, T., Kumbur, E., and Kalidindi, S., 2014, "A Data-Driven Approach to Establishing Microstructure-Property Relationships in Porous Transport Layers of Polymer Electrolyte Fuel Cells," J. Power Sources, 245, pp. 144-153.
- [39] Cecen, A., Dai, H., Yabansu, Y. C., Kalidindi, S. R., and Song, L., 2018, "Material Structure-Property Linkages Using Three-Dimensional Convolutional Neural Networks," Acta Mater., 146, pp. 76–84.
- [40] Xu, H., Li, Y., Brinson, C., and Chen, W., 2014, "A Descriptor-Based Design Methodology for Developing Heterogeneous Microstructural Materials System," ASME J. Mech. Des., 136(5), p. 051007.
 [41] Zhang, Y., Zhao, H., Hassinger, I., Brinson, L. C., Schadler, L. S., and Chen,
- [41] Zhang, Y., Zhao, H., Hassinger, I., Brinson, L. C., Schadler, L. S., and Chen, W., 2015, "Microstructure Reconstruction and Structural Equation Modeling for Computational Design of Nanodielectrics," Integrating Mater. Manuf. Innovation, 4(1), p. 14.
- [42] Bostanabad, R., Zhang, Y., Li, X., Kearney, T., Brinson, L. C., Apley, D. W., Wing, K. L., and Chen, W., 2018, "Computational Microstructure Characterization and Reconstruction: Review of the State-of-the-Art Techniques," Prog. Mater. Sci., 95, pp. 1–41.
- [43] Liu, Y., Greene, M. S., Chen, W., Dikin, D. A., and Liu, W. K., 2013, "Computational Microstructure Characterization and Reconstruction for Stochastic Multiscale Material Design." Comput. Aided Des. 45(1), pp. 65–76.
- chastic Multiscale Material Design," Comput. Aided Des., **45**(1), pp. 65–76.

 [44] Yeong, C., and Torquato, S., 1998, "Reconstructing Random Media—II: Three-Dimensional Media From Two-Dimensional Cuts," Phys. Rev. E, **58**(1), p. 224.
- [45] Yeong, C., and Torquato, S., 1998, "Reconstructing Random Media," Phys. Rev. E, 57(1), p. 495.
- [46] Xu, H., Dikin, D. A., Burkhart, C., and Chen, W., 2014, "Descriptor-Based Methodology for Statistical Characterization and 3D Reconstruction of Microstructural Materials," Comput. Mater. Sci., 85, pp. 206–216.
- [47] Bostanabad, R., Bui, A. T., Xie, W., Apley, D. W., and Chen, W., 2016, "Stochastic Microstructure Characterization and Reconstruction Via Supervised Learning," Acta Mater., 103, pp. 89–102.
- [48] Sundararaghavan, V., and Zabaras, N., 2005, "Classification and Reconstruction of Three-Dimensional Microstructures Using Support Vector Machines," Comput. Mater. Sci., 32(2), pp. 223–239.

- [49] Cang, R., Xu, Y., Chen, S., Liu, Y., Jiao, Y., and Ren, M. Y., 2017, "Microstructure Representation and Reconstruction of Heterogeneous Materials Via Deep Belief Network for Computational Material Design," ASME J. Mech. Des., 139(7), p. 071404.
- [50] Breneman, C. M., Brinson, L. C., Schadler, L. S., Natarajan, B., Krein, M., Wu, K., Morkowchuk, L., Li, Y., Deng, H., and Xu, H., 2013, "Stalking the Materials Genome: A Data-Driven Approach to the Virtual Design of Nanostructured Polymers," Adv. Funct. Mater., 23(46), pp. 5746–5752.
- Polymers," Adv. Funct. Mater., 23(46), pp. 5746–5752.

 [51] Hassinger, I., Li, X., Zhao, H., Xu, H., Huang, Y., Prasad, A., Schadler, L., Chen, W., and Brinson, L. C., 2016, "Toward the Development of a Quantitative Tool for Predicting Dispersion of Nanocomposites Under Non-Equilibrium Processing Conditions," J. Mater. Science, 51(9), pp. 4238–4249.
- [52] Xu, H., Liu, R., Choudhary, A., and Chen, W., 2015, "A Machine Learning-Based Design Representation Method for Designing Heterogeneous Microstructures," ASME J. Mech. Des., 137(5), p. 051403.
- [53] van Lare, M.-C., and Polman, A., 2015, "Optimized Scattering Power Spectral Density of Photovoltaic Light-Trapping Patterns," ACS Photonics, 2(7), pp. 822–831.
- [54] Jin, R., Chen, W., and Sudjianto, A., 2005, "An Efficient Algorithm for Constructing Optimal Design of Computer Experiments," J. Stat. Plann. Inference, 134(1), pp. 268–287.
- [55] Kleijnen, J. P., 2009, "Kriging Metamodeling in Simulation: A Review," Eur. J. Oper. Res., 192(3), pp. 707–716.
- [56] Zhang, X. Y., Trame, M., Lesko, L., and Schmidt, S., 2015, "Sobol Sensitivity Analysis: A Tool to Guide the Development and Evaluation of Systems Pharmacology Models," CPT: Pharmacometrics Syst. Pharmacol., 4(2), pp. 69–79.
- [57] Brigham, E. O., 1988, The Fast Fourier Transform and Its Applications, Prentice Hall, Englewood Cliffs, NJ.
- [58] Chatfield, C., 1996, The Analysis of Time Series: An Introduction, 5th ed., Chapman and Hall, London; New York.
- [59] Panchal, J. H., Kalidindi, S. R., and McDowell, D. L., 2013, "Key Computational Modeling Issues in Integrated Computational Materials Engineering," Comput. Aided Des., 45(1), pp. 4–25.
- [60] Fullwood, D. T., Niezgoda, S. R., and Kalidindi, S. R., 2008, "Microstructure Reconstructions From 2-Point Statistics Using Phase-Recovery Algorithms," Acta Mater., 56(5), pp. 942–948.
 [61] Kadem, B., Cranton, W., and Hassan, A., 2015, "Metal Salt Modified PEDOT:
- [61] Kadem, B., Cranton, W., and Hassan, A., 2015, "Metal Salt Modified PEDOT: PSS as Anode Buffer Layer and Its Effect on Power Conversion Efficiency of Organic Solar Cells," Org. Electron., 24, pp. 73–79.
- [62] Zhao, W., Li, S., Yao, H., Zhang, S., Zhang, Y., Yang, B., and Hou, J., 2017, "Molecular Optimization Enables Over 13% Efficiency in Organic Solar Cells," J. Am. Chem. Soc., 139(21), pp. 7148–7151.

- [63] Li, M., Gao, K., Wan, X., Zhang, Q., Kan, B., Xia, R., Liu, F., Yang, X., Feng, H., Ni, W., and Wang, Y., 2017, "Solution-Processed Organic Tandem Solar Cells With Power Conversion Efficiencies >12%," Nat. Photonics, 11(2), p. 85.
- [64] Wang, A., and Chien, T., 2018, "Perspectives of Cross-Sectional Scanning Tunneling Microscopy and Spectroscopy for Complex Oxide Physics," Phys. Lett. A, 382(11), pp. 739–748.
- [65] Shih, M. C., Huang, B. C., Lin, C. C., Li, S. S., Chen, H. A., Chiu, Y. P., and Chen, C. W., 2013, "Atomic-Scale Interfacial Band Mapping Across Vertically Phased-Separated Polymer/Fullerene Hybrid Solar Cells," Nano Lett., 13(6), pp. 2387–2392.
- [66] Yost, A. J., Pimachev, A., Ho, C. C., Darling, S. B., Wang, L., Su, W. F., Dahnovsky, Y., and Chien, T., 2016, "Coexistence of Two Electronic Nano-Phases on a CH3NH3PbI3–x Cl x Surface Observed in STM Measurements," ACS Appl. Mater. Interfaces, 8(42), pp. 29110–29116.
- [67] Tumbleston, J. R., Ko, D.-H., Samulski, E. T., and Lopez, R., 2010, "Nonideal Parasitic Resistance Effects in Bulk Heterojunction Organic Solar Cells," J. Appl. Phys., 108(8), p. 084514.
- [68] Mikhnenko, O. V., Azimi, H., Scharber, M., Morana, M., Blom, P. W. M., and Loi, M. A., 2012, "Exciton Diffusion Length in Narrow Bandgap Polymers," Energy Environ. Sci., 5(5), p. 6960.
- [69] Mihailetchi, V. D., Xie, H. X., De Boer, B., Koster, L. J. A., and Blom, P. W. M., 2006, "Charge Transport and Photocurrent Generation in Poly(3-Hexylthiophene): Methanofullerene Bulk-Heterojunction Solar Cells," Adv. Funct. Mater., 16(5), pp. 699–708.
- [70] Park, S. H., Roy, A., Beaupré, S., Cho, S., Coates, N., Moon, J. S., Moses, D., Leclerc, M., Lee, K., and Heeger, A. J., 2009, "Bulk Heterojunction Solar Cells With Internal Quantum Efficiency Approaching 100%," Nat. Photonics, 3(5), p. 297.
- [71] Reyes-Reyes, M., Kim, K., and Carroll, D. L., 2005, "High-Efficiency Photo-voltaic Devices Based on Annealed Poly(3-Hexylthiophene) and 1-(3-Methoxy-carbonyl)-Propyl-1-Phenyl-(6,6)C61 Blends," Appl. Phys. Lett., 87(8), p. 083506.
- [72] Park, J.-S., 1994, "Optimal Latin-Hypercube Designs for Computer Experiments," J. Stat. Plann. Inference, 39(1), pp. 95–111.
 [73] Jin, R., Chen, W., and Simpson, T. W., 2001, "Comparative Studies of Meta-
- [73] Jin, R., Chen, W., and Simpson, T. W., 2001, "Comparative Studies of Metamodelling Techniques Under Multiple Modelling Criteria," Computer-Aided Optimal Design of Stressed Solids," Struct. Multidiscip. Syst., 23(1), pp. 1–13.
- [74] Sun, Y., Han, Y., and Liu, J., 2013, "Controlling PCBM Aggregation in P3HT/ PCBM Film by a Selective Solvent Vapor Annealing," Chin. Sci. Bull., 58(22), pp. 2767–2774.